Batch-Operated Condensed Droplet Polymerization to Understand the Effect of Temperature on the Size Distribution of Polymer Nanodomes

Jeremiah James[a, b]
Rong Yang[*] [a]

[a] Robert Frederick Smith School of Chemical and Biomolecular Engineering, Cornell University, Ithaca, NY, 14853, USA
[b] Nancy E. and Peter C. Meinig School of Biomedical Engineering, Cornell University, Ithaca, NY, 14853, USA
[*] ryang@cornell.edu

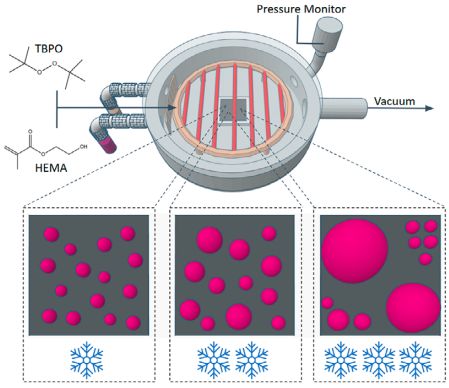

Received: 28.01.2023
Accepted after revision: 12.05.2023
DOI: 10.1055/s-0043-1761311; Art ID: OM-2023-01-0001-OA

Abstract Size-controlled polymer nanodomes (PNDs) benefit a broad cross-section of existing and emerging technologies. Condensed droplet polymerization (CDP) is a vacuum-based synthesis technology that produces PNDs from monomer precursors in a single step. However, the effect of synthesis and processing conditions on the PND size distribution remains elusive. Towards size distribution control, we report the effect of substrate temperature, on which monomer droplets condense, on the size distribution of PNDs. We take a reductionist approach and operate the CDP under batch mode to match the conditions commonly used in condensation research. Notably, despite the rich knowledge base in dropwise condensation, the behavior of nonpolar liquids like a common monomer, i.e., 2-hydroxyethyl methacrylate (HEMA), is not well understood. We bridge that gap by demonstrating that dropwise condensation of HEMA follows a two-stage growth process. Early-stage growth is dominated by drop nucleation and growth, giving rise to relatively uniform sizes with a lognormal distribution, whereas late-stage growth is dominated by the combined effect of drop coalescence and renucleation, leading to a bimodal size distribution. This new framework for understanding the PND size distribution enables an unprecedented population of PNDs. Their controlled size distribution has the potential to enable programmable properties for emergent materials.

Key words: dropwise condensation, nonspherical particles, condensed droplet polymerization, chemical vapor deposition, particle size distribution, programmable materials

Introduction

Polymer nanoparticles have been used broadly across industries from sanitation to construction[1], with their potential impact in emerging areas expanding exponentially. Take targeted drug delivery as an example, polymer nanoparticles were the subject of study in ~90 independent clinical trials conducted under the supervision of the US Food and Drug Administration (US FDA) during 2016 – 2019.[2] Specifically, nonspherical polymer particles like polymer nanodomes (PNDs) have gained increasing interest in healthcare and advanced manufacturing in the past decade due to their optical properties, in vivo uptake profile, emergent assembly, and mechanical properties,[3–6] all of which are distinct from spherical counterparts. In one example, PNDs applied to a fiber optic plasmonic sensor lowered the detection limit of antibody–antigen interactions by an order of magnitude.[3] PNDs have also enabled real-time drug concentration monitoring through the intravenous (IV) tubing during IV injection via surface-enhanced Raman scattering, mitigating 61% of the life-threatening errors during such therapy.[7] The dome shape has been shown to increase spleen uptake of the PNDs, enabling targeted drug delivery via particle shape engineering.[4] The particle dispersion and assembly have also been controlled using nonspherical particles, with a prominent example in suppressing the notorious coffee-ring effect during ink-jet printing.[8]

In the applications mentioned above, the size and size distribution of PNDs emerge as a critical design parameter that dictates the detection sensitivity, the in vivo circulation time, and the group behaviors like jamming. Furthermore, a collection of PNDs with programmed size distribution has the potential to enable new technologies, such as personalized medicine with tailored pharmacokinetics or injectable implants via designed particle packing to balance the per-

meation of nutrients and impact resistance. While existing synthesis approaches have achieved size control for PNDs, there have been few examples of control over the size distribution of PNDs.

A critical limiting factor in the design, synthesis, and manufacturing of PNDs is that existing synthesis techniques are often lengthy and laborious, requiring multiple processes that are hard to scale up.[9,10] For example, PNDs have been formed by heating spherical polymer nanoparticles above their glass transition temperature followed by mechanical deformation, e.g., via stretching or shearing forces.[11] Janus particles have also been leveraged to enable PNDs through chemical modification via click chemistry.[12] In contrast to these multi-step and often multi-day procedures, an emerging vacuum-based synthesis technique, namely condensed droplet polymerization (CDP), has demonstrated the swift synthesis of PNDs using a single vacuum-based procedure. By avoiding liquid processing, lengthy purification steps are eliminated entirely. Indeed, CDP produces PNDs from the monomer precursors in a single step within minutes.

Distinct from nearly all the other vacuum-based synthesis techniques, such as chemical vapor deposition (CVD) and molecular layer deposition (MLD),[13] CDP operates under oversaturated conditions for the precursor (i.e., monomer). It comprises two simple steps that occur in a single vacuum chamber: (i) dropwise condensation of monomers on a low surface energy substrate material such as poly (1*H*,1*H*,2*H*,2*H*-perfluorodecyl acrylate) (pPFDA),[14] which is actively cooled; and (ii) free radical polymerization of the condensed monomer droplets. The average diameter of the PNDs is controlled, e.g., in the range of 200 to 800 nm in a previous work,[1] using real-time and in-situ characterization techniques, including interferometry and a long-focal-range reflective microscope. The aspect ratio of the PNDs is tunable by manipulating the surface energy of the solid substrate. However, despite the facile synthesis and tunable PND morphology, the effects of synthesis conditions on the PND size distribution remain elusive. For example, PND size distribution beyond the demonstrated normal distribution has not been achieved.[1]

To address the gap in PND synthesis, here we focus on the effect of the solid substrate temperature on the monomer droplet growth kinetics, based on which we develop a framework of two-stage condensation kinetics to help understand the emergence of particle size distribution during CDP. 2-Hydroxyethyl methacrylate (HEMA) was chosen as a model monomer due to its biocompatibility and its demonstrated applications in sustained, targeted, or local drug delivery.[4,15–18] We believe that the size of the condensed monomer droplets largely determines the size of the resulting PNDs. The two key parameters that govern the monomer condensation are the monomer partial pressure in the vacuum chamber (P_M) and the temperature of the cooled substrate (T_s) on which the monomer is condensed (Figure 1).[15] For a given T_s, monomer condensation (e.g., rate of drop nucleation and growth) can be controlled by manipulating P_M,[16] and vice versa. We chose to perform CDP under constant P_M and batch mode while systematically varying T_s. This choice is informed by the plethora of the existing literature on dropwise condensation,[17] which predominantly studied the condensation mechanisms and kinetics under batch conditions while varying the condensation temperature. For example, the broadly adopted Rose model was established by varying the vapor–substrate temperature difference,[18] which led to distinct size distributions of the condensed water droplets. By performing CDP under similar batch conditions, we could build upon the rich existing theories on dropwise condensation to formulate an initial framework to understand droplet growth of nonpolar liquids such as monomers.

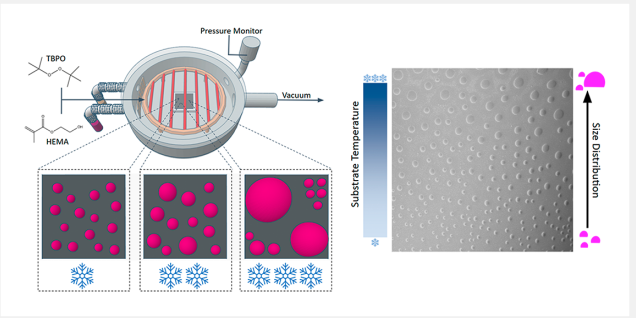

Figure 1 Left: a schematic of the CDP reactor consisting of monomer feed through lines, a capacitance manometer coupled with a throttling valve to maintain constant monomer partial pressure (P_M), a thermoelectric cooling (TEC) plate to precisely control the substrate temperature (T_s), and a heated filament array to generate free radicals (by thermally breaking down *tert*-butyl peroxide, TBPO) that initiate polymerization. The monomer, 2-hydroxyethyl methacrylate (HEMA), is delivered into the chamber and condensed on a substrate cooled by the TEC plate. The PND size distributions reflect the two-regime condensation kinetics, with the size distribution at high T_s dominated by monomer drop nucleation (hence close to lognormal distribution) and that at low T_s dominated by drop coalescence and renucleation (hence bimodal). Right: a scanning electron microscopy (SEM) image taken from a single substrate, with a temperature gradient along the substrate (in the vertical direction) during condensation. That gradient was created by lifting the substrate slightly off the cooling module.

Our results show that the maximum attainable PND size increases as T_s decreases. The PND size distributions map well onto the well-established two-regime growth mechanism of droplets on a nonwetting surface, with the early growth dominated by vapor absorption and late growth dominated by drop coalescence.[19,20] At the higher T_s values that we studied (i.e., 30 °C and 27 °C), the PND size distribution is close to a lognormal distribution, reflective of the early-stage droplet growth dominated by vapor absorption. At the lower T_s values studied (i.e., 24 °C and 21 °C), the PNDs

demonstrate a bimodal distribution, reflective of the late-stage monomer droplet growth dominated by the combined effects of droplet coalescence and renucleation.[21,22] These findings establish a framework for understanding the emergence of PND size distributions and the effect of system temperature on size distribution, which will inform future research into the dropwise condensation kinetics of nonpolar liquids. This work also sets the stage to produce PNDs with programmable size distributions and group behaviors, with enormous impact in nanomedicine, drug delivery and biomaterials, sensing, nano-optics, and advanced manufacturing technologies.[5,23–25]

Results and Discussion

Synthesis of PNDs Using Batch-Operated CDP Technology

PNDs made of poly(HEMA) (pHEMA) were obtained using batch-operated CDP (Figure 2), as detailed below. A substrate with low surface energy was used to obtain the desired dropwise condensation of the monomer HEMA.[1] To ensure the low surface energy, a silicon wafer was coated by pPFDA that was synthesized using initiated CVD (iCVD) (see Figure S1A in the Supporting Information for its X-ray photoelectron spectroscopy (XPS) spectrum and the Experimental section for deposition conditions). We have demonstrated previously that the contact angle of liquid HEMA on a pPFDA coating is 86.5° ± 1.6°,[1] which enables dropwise condensation of HEMA on pPFDA while avoiding small droplets from hiding underneath large droplets, which often occurs when the contact angle exceeds 90° and complicates the image analysis to obtain the size distribution.[26]

The batch CDP process started with delivering vaporized HEMA into the vacuum chamber (totaling approximately $2.7 \pm 0.8 \times 10^{-5}$ mol) to reach a P_M of approximately 100 mTorr. Subsequently, T_s was reduced to the desired temperature (i.e., 21 °C, 24 °C, 27 °C, or 30 °C) and maintained there for 5 minutes. During this step, dropwise condensation of HEMA occurred on the substrate, which was monitored in real time using an in-situ long-focal reflective microscope. Droplets were allowed to grow (and/or coalesce) for the duration of the 5 minutes, and at the end of which, a vapor flow of an initiator, i.e., *tert*-butyl peroxide (TBPO), was introduced at ~0.6 sccm for 1 minute. TBPO generates free radicals upon passing through a heated zone inside the vacuum chamber (generated by a resistively heated filament array kept at approximately 270 °C). The radicals initiate free-radical polymerization in the condensed monomer droplets and convert them into solid PNDs. The polymerization proceeded for an additional minute before the chamber was evacuated, marking the end of a batch-operated CDP cycle. Previous work polymerized the monomer droplets for merely 45 seconds and observed complete polymerization.[1] We adopted the total polymerization time of 2 minutes here to ensure that all monomer droplets were fully polymerized. The PND size distribution can thus be attributed to the condensation kinetics of monomer droplets.

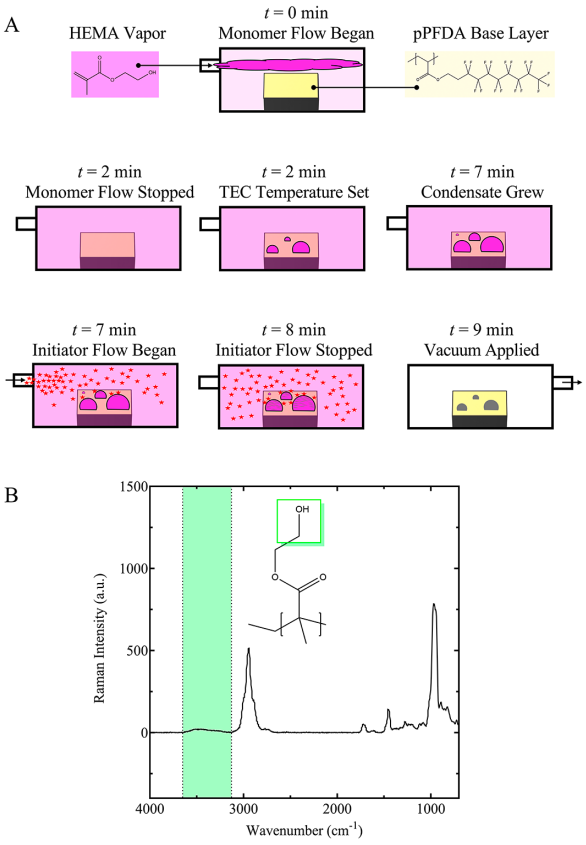

Figure 2 (A) Schematic showing the experimental procedure to synthesize the PNDs. HEMA and pPFDA are indicated by pink (e.g., the monomer vapor and condensed droplets) and yellow, respectively; free radicals are indicated by red stars. The HEMA droplets formed atop a pPFDA-coated substrate that was cooled by a TEC plate, and the HEMA droplets were subsequently polymerized to form PNDs. (B) Confocal Raman microscopy was applied to obtain the spectrum of the pHEMA PNDs on a pPFDA-coated substrate; the broad peak highlighted in green signifies the O–H stretching characteristic of pHEMA.

The chemical/elemental composition of the PNDs was confirmed using confocal laser Raman microscopy (Figure 2), XPS (Figure S1B), and Fourier-transform infrared spectroscopy (FTIR; Figure S1C). As an example, the composition of PNDs synthesized at T_s ~21 °C is detailed below. Using the 100 x objective lens focused on a PND that was ~1 µm in diameter, the Raman spectrum revealed the characteristic O–H stretching of pHEMA, signified by a broad peak from 3130 to 3650 cm^{-1} (Figure 2, green-highlighted region).[27,28] The carbonyl stretching at 1730 cm^{-1},[29] CH_2/CH_3 stretching

at 2850 to 3000 cm^{-1},[30] and C–C/C–O stretching at 1000 to 1400 cm^{-1} also corroborated the successful obtainment of pHEMA.[31,32] The CF_2 and CF_3 stretching from the pPFDA base layer may also contribute to the peaks at 1000 to 1400 cm^{-1},[33,34] as the sampling area of the Raman microscope we employed was 1 µm by 1 µm and greater than the area of a single PND (< 1 $µm^2$).

We performed end-group analysis on the pHEMA PNDs (using those synthesized at T_s ~21 °C as an example) to gain insight into the initiation and termination mechanisms at play during batch CDP. End-group analysis data were obtained using MALDI-TOF and analyzed using the Polymerix software by altering the alpha and omega end groups to identify the most significant *m/z* peak (Figure S2). Results showed that pHEMA chains in the PNDs predominantly presented methyl end groups, indicating substantial β-scission during the thermolysis of TBPO (Figure S2). Briefly, when TBPO is exposed to temperatures above 270 °C (the condition used in this paper), in addition to the homolysis of TBPO that generates *tert*-butoxyl radicals, β-scission of the *tert*-butoxyl radicals also occurs, which gives rise to methyl radicals (and acetone as a byproduct).[35] Notably, no HEMA end groups were observed (which has been observed in previous work).[1] That absence of HEMA end groups implies that the batch CDP likely suppressed chain transfer during polymerization, the precise origin of which will be an important focus of our future studies. The dominant polymeric chain showed a number average molecular weight (M_n) of 4314 Da, weight average molecular weight (M_w) of 5214 Da, and a polydispersity of 1.209.

Effect of Substrate Temperature on PND Size and Size Distribution

To understand the effect of substrate temperature (T_s) on the size distribution of the PNDs, we synthesized PNDs under different T_s while holding all the other synthesis conditions unchanged (e.g., P_M, filament temperature, experimental procedure). The PND size distribution was captured using scanning electron microscopy (SEM) and quantified by analyzing the dome sizes using ImageJ. Manual adjustments to the ImageJ analysis were made until all PNDs on the SEM image were included in the analysis (see the Experimental section for details).

Before presenting and discussing the PND size distribution results, we believe it is crucial to review the relevant condensation theories, which serve as the foundation for our interpretation of the size distribution data and the underlying kinetic processes. Specifically, the size distribution results below will be discussed in the context of the Rose model and its derivative theories. In its simplest form, condensation can be described as having multiple generations. The first-generation droplets appear randomly on the surface at the onset of condensation, described by Rose et al. using the nucleation site density.[36] Mu et al. further supported this theory and demonstrated the influence of the surface fractal dimension on nucleation sites.[37] As the first-generation droplets grow, droplet coalescence begins to occur, and with every coalescence event, more substrate area is freed up from underneath a liquid droplet. For example, if one droplet coalesces with another of equal radii, the resulting droplet would occupy an area that is 20% less than the two parent droplets combined (Figure S3). This opens up free space on the cold substrate. The re-exposure of the substrate surface subsequently leads to nucleation of fresh droplets, often termed a second generation.[16] However, the term generation may be misleading as this cyclic process of coalescence and renucleation results in the continuous formation of droplets (and not discretized generations as the description implies). This continuous droplet formation has been confirmed by monitoring the surface coverage of a substrate by condensed droplets, which quickly ramps up and stabilizes at a constant value throughout the condensation process.[38] Below, we instead adopt the nomenclature of first-generation droplets and non-first-generation droplets and the treatment that if a non-first-generation droplet coalesces with a first-generation droplet, the resulting drop remains in the first-generation population, with the rationale for this treatment explained below.

Using a T_s of 30 °C led to a relatively narrow size distribution, with 100% of PNDs ranging from 44 nm (minimum) to 112 nm (maximum) in Feret diameter (Figure 3A – C). The

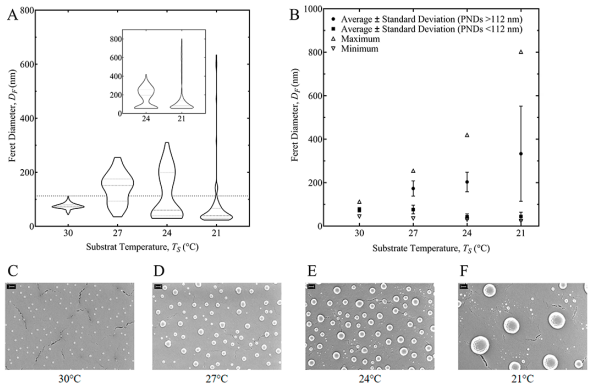

Figure 3 Size distributions of pHEMA PNDs obtained at T_s of 21 °C, 24 °C, 27 °C, and 30 °C. (A) A violin plot of the Feret diameters of the PNDs obtained at each T_s (extracted from SEM images with a width of 5 µm); the dashed line shows the cutoff between small and large PNDs, i.e., 112 nm; the inset shows the size distributions of PNDs obtained at 24 °C and 21 °C that were extracted from SEM images with a width of 20 µm to capture a representative number of larger PNDs (see Figure S4). (B) Average and standard deviation of the small and large PNDs, and the maximum and minimum Feret diameter obtained at each T_s. (C – F) SEM images (scale bar = 200 nm) of the PNDs obtained at each T_s on a pPFDA-coated substrate.

PNDs were lognormally distributed with a mean of 72 nm and a shape parameter (i.e., the geometric standard deviation of the log of the distribution) of 1.2 (Table S1). This lognormal distribution is consistent with the molecular clustering physical model of steam condensation, which predicts that vapor molecules become clusters with lognormal size distribution in the bulk vapor phase before condensing onto a cooled surface.[39] Experimentally, pre-coalescing water droplets with sizes up to several microns have been shown to follow the molecular clustering model, demonstrating lognormal distributions. In our experiment, the lognormal size distribution of pre-coalescing monomer droplets was subsequently transferred to the PNDs through polymerization. To further illustrate the difference among the PND size distributions obtained under each T_S, we calculated the substrate area occupied by each PND size group (Figure 4). At T_S of 30 °C, the substrate surface coverage was entirely due to the PNDs that reside within the lognormal distribution, with an areal density of 7 PNDs/μm^2.

A bimodal distribution started to emerge under the T_S of 27 °C (Figure 3A, 3B, and 3D). The minimum and maximum Feret diameters were 35 and 255 nm, respectively. Compared to T_S = 30 °C, the smallest PNDs synthesized at 27 °C were 20% smaller, and the largest 130% bigger. Interestingly, the group of PNDs with Feret diameters less than 112 nm demonstrated a lognormal distribution with an average of 82 nm and a shape parameter of 1.3 (Table S1), close to those obtained at T_S = 30 °C. This resemblance hints at a similar nucleation-growth mechanism during the early-stage condensation of monomer. In addition to this population, a second group of larger drops emerged (here defined as drops with Feret diameter > 112 nm), with an average Feret diameter of 166 nm and a shape parameter of 1.3 when regressed using a lognormal function (Table S2). As discussed above, monomer droplets can grow through vapor absorption or drop coalescence, and Figure 3(A and D) indicates that both processes were likely occurring at 27 °C. The lognormal function was chosen here for the population with larger Feret diameters because previous work has shown that double lognormal distribution accurately captures the bimodal distribution that emerges from simultaneous nucleation and coalescence on a horizontal surface.[40] The noncircular shape of the larger PNDs (Figure 3D) also supports the occurrence of drop coalescence due to contact line pinning,[41] whereas the circular domes likely grew through vapor absorption. When comparing the areal occupancy (Figure 4B), the small drops (< 112 nm) occupied merely 8% of the PND-covered substrate area, while the large drops (> 112 nm) occupied 92% of the area.

Lowering the T_S to 24 °C (Figure 3A, 3B, and 3E) further broadened the PND size distribution. Compared to 27 °C, the minimum drop size was reduced by 17% to 29 nm, and the largest PND was enlarged by 65% to 420 nm. Again, two distinct lognormal populations emerged, with an average

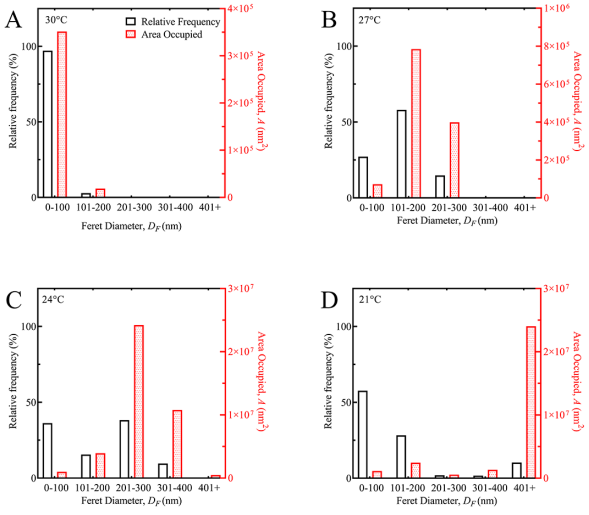

Figure 4 Histograms comparing the relative frequency (i.e., the fractional number density) of PNDs in each size group versus their occupied area, obtained at T_S of (A) 30 °C, (B) 27 °C, (C) 24 °C, and (D) 21 °C.

Feret diameter of 40 and 235 nm, and a shape parameter of 1.4 and 1.4, respectively (Figures 3B, 3E and S4 and Tables S1 and S2). Figure 4C shows that large PNDs (> 112 nm) occupied 92% of the total PND-covered area, whereas small PNDs (< 112 nm) occupied 8% of the total area. The size distribution and areal occupancy combined indicate that droplet coalescence was more prevalent under T_S = 24 °C compared to 27 °C, as coalescence has been shown to yield larger droplet sizes, reduced number density of large droplets, and a broader size distribution.[42] The increased number density of small PNDs hints at the greater presence of non-first-generation droplets, which formed on the substrate area freed up due to nearby coalescence.

At T_S ~21 °C, large PNDs with diameters up to 800 nm were observed, as shown in Figure 3(A, B, and F). Compared to 24 °C, the minimum drop size was reduced by 20% to 23 nm, and the largest PND was enlarged by 90% to 800 nm. While PNDs with Feret diameters greater than 112 nm occupied 94% of the PND-covered substrate area, their number density was merely 1 PND/μm^2. As such, the distribution function of the PND Feret diameter under T_S ~21 °C was dominated by small PNDs (< 112 nm) (Figure 3A). Enhanced coalescing compared to 24 °C was likely the reason for the reduced number density of large drops. Similar to 24 °C, the small PNDs obtained at T_S ~21 °C exhibited a lognormal distribution with an average Feret diameter of 40 nm and a shape parameter of 1.7 (Figure 3F and Table S1). The Feret diameters of large PNDs (> 112 nm) were largely randomly distributed. A normal distribution regression yielded an average diameter of 333 nm and a standard deviation of

219 nm (Figure S4). This distribution, combined with the small number density of large PNDs, likely reflects the stochastic nature of the coalescence of monomer drops, as coalescence can occur between droplets of any size.[43]

It has been well accepted in condensation-based heat transfer research that lowering the solid substrate temperature increases the density of water droplet nucleation sites (under constant steam temperature).[44–46] While the PND density data presented above do not follow a clear trend with respect to T_S because they are not a direct result of droplet nucleation but rather the combined effect of nucleation and coalescence, theory predicts that the density of small drops (e.g., with Feret diameter < 112 nm) should increase as T_S decreases. To eliminate the subjectivity in choosing a group of small PNDs to calculate their number density, we instead calculated the average distance between small PNDs under each T_S to assess the effect of T_S on the density of nucleation sites. Assuming small drops represent nucleation sites, we obtained an average separation distance of 370 nm ($N = 106$) at $T_S = 30\,°C$, which decreased to 150 nm ($N = 81$) at $T_S = 21\,°C$ (analysis depicted in Figure S5).

In addition to the increasing density of nucleation sites under lower T_S, coalescence was also enhanced by a faster condensation speed and more rapid droplet growth at lower T_S. Previous research has shown an increase of 40% in the droplet growth rate upon a 10 °C decrease in T_S.[47] Consistent with the previous reports showing the accelerated progression along the condensation cycles at a lower T_S, our results demonstrated that the particle size distribution obtained after 2.5 minutes of condensation at $T_S = 21\,°C$ was similar to those obtained after 5 minutes at $T_S = 30\,°C$ and 27 °C (Figure 3). Thus, by shortening the time of condensation on a substrate kept at a lower temperature, we achieved a PND size distribution similar to those obtained on warmer substrates, thus corroborating the condensation literature (Figure S6).[44]

Occurrence of Drop Coalescence during Condensation and Effects on PND Size Distribution

A simple yet effective way to identify the occurrence of drop coalescence is to rank the PND sizes from smallest to largest under each T_S (Figure 5). As such, the coalescence of drops would be manifested by step changes and discontinuity in the ranking curve, whereas a uniform size distribution of PNDs would lead to a smooth and continuous ranking curve.[40] We emphasize that the curves represent the small-to-large ranking of the diameter of the PNDs, and thus it does not reflect the growth rate of the monomer drops under each substrate temperature.

We first validated that interpretation by examining the ranking curve obtained at $T_S = 30\,°C$, which was continuous and relatively constant. That ranking curve shape implied

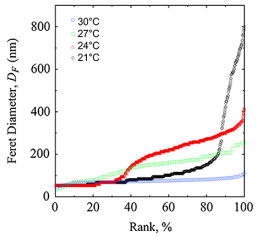

Figure 5 Ranked curves for the Feret diameters of the PNDs obtained at T_S of 30 °C ($n = 106$), 27 °C ($n = 81$), 24 °C ($n = 1578$), and 21 °C ($n = 879$).

minimal coalescence under this condition, consistent with the SEM images of the PNDs formed under 30 °C (Figure 3C). The ranking curve demonstrated a slight slope, which we attributed to the stochastic nature of heterogeneous nucleation, i.e., monomer drops nucleated at different times had different growth times and thus demonstrated different sizes.

Interestingly, that smooth and steady lower segment of the ranking curve was observed under all T_S, occupying varying portions of the total population. At 27 °C, the ranking curve followed a similarly smooth and continuous shape as that at 30 °C, hinting at their similar growth mechanism (i.e., nucleation and growth via adsorption of vapor-phase monomer). The slope of the ranking curve was greater at 27 °C than at 30 °C, which we attributed to (i) the more rapid rate of condensation at 27 °C (that magnified the stochasticity of drop nucleation) and (ii) the greater surface area of the monomer drops at 27 °C than at 30 °C, leading to faster growth through monomer surface adsorption. Discontinuity of the ranking curve was observed at 27 °C for the largest 6% of the domes, possibly due to drop coalescence or simply the small sample size in this range.

Similarly, at 24 °C, the smallest 31% of the domes likely underwent nucleation and growth without significant coalescence, leading to a uniform size distribution and thus a small slope of the ranking curve in this segment. A pseudo-step change in the ranking curve was observed in the 70 to 170 nm range, which implied drop coalescence at small drop sizes, likely due to the low substrate temperature and high drop density, as evident from the SEM image (Figure 3E). Intriguingly, another pseudo-plateau was observed with dome sizes ranging from 150 to 330 nm, averaging 242 ± 45 nm. The slope of this pseudo-plateau is larger than that at 27 °C, indicating the greater heterogeneity in the PND size distribution in this range. We attributed that greater heterogeneity to the fact that at $T_S = 24\,°C$, the droplet growth is driven by a combination of vapor absorption and drop coalescence. Drop coalescence is known to broaden the drop size distribution in the condensation literature.[44]

The most apparent coalescence occurred under T_s ~21 °C, which gave rise to a nearly vertical ranking curve for PNDs with Feret diameters over 200 nm. A complete discontinuity was observed in the 260 to 330 nm range, which serendipitously corresponds to the coalescence of two drops with a diameter of 260 nm giving rise to one drop with a diameter of 327 nm. It also matches the areal density of 1 PND per 370 nm^2 observed at 30 °C, i.e., the nucleation site density prior to coalescence. While this simple explanation likely does not fully account for all the possible reasons for this gap, it hints at a critical size at which droplets experience heightened chances to undergo a coalescing event. The ranking curve at 21 °C nonetheless demonstrated a smooth and continuous segment (i.e., for the first 37 percentiles), just like that for 24 °C, 27 °C, and 30 °C, which we attributed to the fresh nucleation and growth of monomer drops on the substrate space that was freed by coalescing of larger drops.

Although not a focus of this report, the polymerization step during CDP may also affect the final PND size distribution. For example, incomplete polymerization of a large monomer drop may lead to shrinking of the dome size upon removal of unreacted monomer (e.g., by evacuating the vacuum chamber). It is likely that dome shrinking occurred in this study, especially at lower T_s, as seen by the blank space observed in the SEM image at T_s = 21 °C, which outlined a boundary between the populations of large and small PNDs that may not be explained by simple renucleation that follows a drop-coalescence event. Similar morphologies have been observed in the condensation literature.[26] The blank areas surrounding large liquid drops have been attributed to the evaporation of the condensed liquid, typically achieved by warming the substrate and thus shrinking the large drops.[48,49] In the context of CDP, evaporation of the condensed monomer could occur at the end of the polymerization step, when the reactor chamber was evacuated. The large domes with blank areas around them likely experienced incomplete polymerization and shrinkage upon application of vacuum. Nevertheless, we emphasize that the current manuscript focuses on the effect of monomer condensation on the PND size distribution, and we reserve a detailed investigation into the effect of incomplete polymerization for a future study.

While the density discrepancy between the HEMA monomer and pHEMA could contribute to the aforementioned blank space observed in the SEM image at T_s = 21 °C, it is likely not the sole explanation. The density of a polymerizing HEMA drop could increase from 1.12 g/mL (for HEMA monomer) to 1.26 g/mL (for pHEMA),[50,51] and the corresponding volume change thus accounts for a small fraction of the blank space as shown in Figure S7.

Furthermore, varying T_s may also affect the rate of polymerization. To estimate that effect, we applied the Arrhenius law using the activation energy reported in the literature for HEMA and the T_s values.[51] The propagation constant (k_p) for HEMA can be reduced by ~23% (Figure S8) as the substrate temperature was decreased from 30 °C to 21 °C. As such, we assume the overall effect of k_p on PND size distribution (under conditions used here) is minimal, which is further corroborated by the observation of larger PNDs at lower T_s, indicating that the monomer condensation step dominates the PND size and size distribution. Furthermore, the effect of lower k_p under lower T_s may be offset by the larger surface area of each monomer drop obtained under lower T_s, enabling the capture of more free radicals and hence a greater rate of initiation.

Conclusions

Taken together, the PND size distributions obtained at the four T_s values (21 °C, 24 °C, 27 °C, and 30 °C) demonstrate the potential to program PND size distribution using the batch-CDP synthesis approach and by manipulating the temperature at which monomer condensation occurs. Higher T_s (e.g., 30 °C) leads to a slower rate of condensation and a lognormal distribution of PND sizes, which resembles early-stage condensation governed by surface nucleation and drop growth via absorption of vapor monomer. That lognormally distributed drop size is, in turn, recapitulated in the PND size distribution as the monomer drops are converted to PNDs via free-radical polymerization. A bimodal distribution emerges as T_s is reduced to 27 °C, 24 °C, and 21 °C. Interestingly, all three T_s values lead to a population of small PNDs with an average size close to those obtained under T_s = 30 °C, which points to the continuous nucleation and condensation on the solid surface throughout the observed period. In addition to this population, the particles synthesized under T_s of 27 °C, 24 °C, and 21 °C include a second population of larger PNDs, with the average size increasing and the distribution broadening as T_s decreases. We attribute this population of larger PNDs to the coalescence of monomer droplets during late-stage condensation, which has been frequently observed in past studies of dropwise condensation.[52] The maximum Feret diameter observed among the PNDs obtained under each T_s increases as T_s decreases, which roughly doubles upon each decrease of T_s by 3 °C, i.e., 112 nm for T_s ~30 °C, 255 nm for T_s ~27 °C, 420 nm for T_s ~24 °C, and 800 nm for T_s ~21 °C, respectively. The minimum Feret diameter obtained under each T_s decreases by ~20% upon each decrease of T_s by 3 °C.

This report builds upon the plethora of condensation research conducted using water and at the macroscopic scale and illustrates that the dropwise condensation of nonpolar liquids, such as HEMA, follows a similar two-stage growth process to water. It establishes an initial framework to understand the condensation kinetics of nonpolar nano/micro-drops and illuminates the process–property correlations that will guide the selection of synthesis parameters

to obtain targeted PND size and size distributions. The PNDs with programmable size distribution have the potential to revolutionize infrastructure, consumer products, healthcare, and robotics.

Experimental Section

Materials

All purchased chemicals were used as received. The base layer was synthesized using 1*H*,1*H*,2*H*,2*H*-perflurodecyl acrylate (PFDA; Sigma Aldrich, 97%) polymerized via TBPO (Sigma-Aldrich, 98%). Nanodomes were synthesized using monomer HEMA (Sigma-Aldrich, > 99%).

Methods

The PNDs were synthesized using the CDP technique, as described below, and characterized for chemical composition using XPS, Raman microscopy, and FTIR. The molecular weight and end-group analysis were determined using a Bruker autoflex maX to obtain the MALDI-TOF spectra. Detailed morphology of PNDs was obtained via SEM, and particle size and size distribution were determined using ImageJ. All data manipulation and graphing were conducted using Prism9.

Procedures

Base layer preparation: All purchased chemicals were used as received. Substrates used in CDP were silicon (Si) wafers coated with a base layer of pPFDA, synthesized using monomer PFDA (Sigma-Aldrich, 97%). Briefly, a silicon wafer was first placed onto the stage in an iCVD reactor chamber to deposit the pPFDA film. The stage was set to 30 °C during iCVD using a recirculating chiller (Thermo Scientific), and the chamber was evacuated to base pressure (< 5 mTorr) by connecting to a vacuum pump. A glass jar containing PFDA was heated to 80 °C. PFDA was vaporized and metered into the chamber at 0.25 sccm using a needle valve. Argon and TBPO were also delivered to the chamber at 0.9 sccm and 1.6 sccm, respectively, using mass flow controllers. The throttling valve was programmed to maintain a chamber pressure of 400 mTorr. Positioned 3 cm above the substrate was a filament array of 0.5 mm copper/nickel wire (55% Cu/45% Ni, Goodfellow) set to 300 °C by an external DC power supply to thermally decompose TBPO into *tert*-butoxyl and methyl radicals, which initiate polymerization on the wafer surface. The base layer thickness was observed in real time using an interferometer equipped with a 633 nm helium–neon laser (JDS Uniphase). When a thickness of 100 – 200 nm was reached, the reaction was halted by ceasing the flow of all reactants and evacuating the chamber. Due to tendency of pPFDA to form crystalline domains, hence creating roughness on the nanoscale,[53] the pPFDA-coated substrate was placed into an oven set at 80 °C for 1 hour to reduce the roughness. Next, the flat pPFDA wafer was removed from the oven, cooled, and stored until further use.

Synthesis of PNDs: An iCVD reactor chamber and monomer delivery channels were heated to maintain a temperature between 90 and 100 °C to direct condensation solely on the base layer. The chamber stage was held at 65 °C during CDP. Precise temperature manipulation of the monomer-condensing surface was achieved using a thermoelectric cooler (TEC; VT-127-1.0-1.3-71, TE Technology). To ensure effective heat transfer under vacuum, the TEC was secured to the stage using a ceramic thermal compound (GC ELECTRONICS). An external DC power supply (Extech) was connected to the TEC using copper feedthroughs. The substrate, a pPFDA-coated silicon wafer, was secured atop the TEC using the ceramic thermal compound. Kapton tape was used to attach a thermocouple to the substrate for real-time temperature readings. The chamber was then sealed and brought down to vacuum (< 5 mTorr) by fully opening the throttling valve. The filament array was then heated to 300 °C. A glass monomer jar containing HEMA (Sigma-Aldrich, > 99%) was heated to 105 °C, and the HEMA vapor was delivered continuously to the vacuum chamber for 2 minutes. The TEC was then cooled to the desired temperature (21 °C, 24 °C, 27 °C, 30 °C) and maintained for 5 minutes. TBPO was delivered subsequently for 1 minute. After ceasing the TBPO flow, the chamber remained isolated for 1 minute of further polymerization. Finally, to end the reaction, the TEC and the filament array were turned off, and the throttling valve was opened fully to bring the chamber to base pressure (< 5 mTorr).

Sample characterization: PNDs with Feret diameters of ~1 µm were used (synthesized at T_s = 21 °C) in XPS. The XPS used was a Scienta Omicron ESCA-2SR Spectrometer with an operating pressure of 1×10^{-9} Torr. Monochromatic Al Kα X-rays (1486.6 eV) were used, and photoelectrons were collected from a 1.1 mm diameter analysis spot. Photoelectrons were gathered at a 90° emission angle with a source-to-analyzer angle of 54.7°. A hemispherical analyzer determined electron kinetic energy using a pass energy of 200 eV for wide/survey scans and 50 eV for high-resolution scans. A flood gun was used for charge neutralization. Raman microscopy was performed using a WITec alpha300 R Raman imaging microscope. A 532 nm laser was used to collect spectra with a power of approximately 1 mW and a 100 x objective lens. A spectral grating of 1200 mm^{-1} was used with a resolution of 3 cm^{-1} using 300 lines mm^{-1} and an accumulation of 10 scans of 10 seconds each. Using the same sample, FTIR spectra were collected. Data were collected using a Bruker VERTEX Series V80v spectrometer in the transmission mode, a mercury cadmium telluride detector, and FTIR

spectra of nanodomes on a pPFDA-coated Si wafer were collected. The spectra were recorded across a range of 4000 – 1000 cm^{-1} (4 cm^{-1} resolution) and were averaged over 128 scans. The background-corrected spectra were obtained by subtracting the spectra of a bare Si wafer and then baseline-corrected. Three batches of PNDs with Feret diameters of ~1 µm were used in MALDI-TOF analysis. The PNDs were dissolved in methanol and vortexed with a solution (20 mg/mL ethanol) of α-cyano-4-hydroxycinnamic acid (CHCA, Sigma-Aldrich, > 98%), and Milli-Q water at the ratio of 1 : 1 : 0.4. Next, 3 µL mixture was pipetted onto a MALDI-TOF analysis plate and allowed to air dry. A Bruker autoflex maX in positive reflectron mode was used to collect MALDI-TOF spectra. The collected spectra were baseline-subtracted and analyzed using Polymerix (Sierra Analytics). The homopolymer analysis in Polymerix was used to determine the dominant series of alpha and omega end groups. Analysis was performed up to $m/z = 10000$, beyond which peaks were indistinguishable from background noise. SEM was performed on a Zeiss GeminiSEM 500. Samples were coated with gold/palladium prior to imaging. Images were taken using an acceleration voltage of 1 kV. Acquired images were imported into ImageJ (National Institutes of Health, Bethesda, MA), and PNDs were analyzed for diameter, area, surface coverage, and count. Non-PND features were manually removed; threshold was set manually to enable recognition of PNDs from background; PNDs were analyzed using the Analyze Particles tool.

Prism9 (GraphPad Software Inc., La Jolla, CA) was used for all data graphing and fitting. For T_s of 30 °C and 24 °C, lognormal distribution fits were applied to PNDs binned into four bins for small Feret diameters (< 112 nm) and large Feret diameters (> 112 nm) yielding R^2 values of > 0.99. For T_s of 24 °C and 21 °C, the small PNDs were fit to a lognormal distribution as described above. The lognormal distribution was also applied to large PNDs obtained under T_s of 24 °C, with four frequency bins and an R^2 value of > 0.99. ChemDraw (PerkinElmer, Waltham, MA) was used to create all chemical structures. Tinkercad (Autodesk, Mill Valley, CA) was used to create a 3D rendering of the reactor chamber used in this work.

Funding Information

This material is based upon work supported by the National Science Foundation (NSF) through the Faculty Early Career Development Program (CAREER) under Grant No. CMMI-2144171. J.J. is supported by the NSF Graduate Research Fellowship Program (GRFP) under Grant No. DGE-2139899 and the Cornell Engineering Lance R. Collins Fellowship.

Acknowledgment

Analytical methods involved the use of the Cornell Center for Materials Research (CCMR) Shared Facilities, which are supported through the NSF MRSEC program (DMR-1719875). The authors acknowledge Dr. Trevor Franklin for his helpful discussions on the CDP mechanism.

Supporting Information

Supporting Information for this article is available online at https://doi.org/10.1055/s-0043-1761311.

Conflict of Interest

A provisional patent (PCT/US2022/74425) has been filed, which may include the discoveries reported in this manuscript, with the authors as co-inventors.

References

(1) Franklin, T.; Streever, D. L.; Yang, R. *Chem. Mater.* **2022**, *34*, 5960.
(2) Anselmo, A. C.; Mitragotri, S. *Bioeng. Transl. Med.* **2019**, *4*, e10143.
(3) Kim, H.-M.; Lee, H.-Y.; Park, J.-H.; Lee, S.-K. *ACS Sens.* **2022**, *7*, 1451.
(4) Decuzzi, P.; Godin, B.; Tanaka, T.; Lee, S.-Y.; Chiappini, C.; Liu, X.; Ferrari, M. *J. Controlled Release* **2010**, *141*, 320.
(5) Steltz, E.; Mozeika, A.; Rembisz, J.; Corson, N.; Jaeger, H. M. *Jamming as an Enabling Technology for Soft Robotics*. In *Proceedings of the SPIE 7642, Electroactive Polymer Actuators and Devices*. Bar-Cohen, Y., SPIE: San Diego, CA, **2010**, 764225.
(6) Guo, Y.; Wassgren, C. R.; Hancock, B. C.; Ketterhagen, W. R.; Curtis, J. S. *Phys. Fluids* **2013**, *25*, 63304.
(7) Wu, H.-Y.; Cunningham, B. T. *Nanoscale* **2014**, *6*, 5162.
(8) Yunker, P. J.; Still, T.; Lohr, M. A.; Yodh, A. G. *Nature* **2011**, *476*, 308.
(9) Kinsyo, T.; Nakanishi, H.; Hirai, K.; Noda, H.; Takikawa, T.; Yahiro, S. *Polym. J.* **2017**, *49*, 593.
(10) Karthaus, O.; Mikami, S.; Hashimoto, Y. *J. Colloid Interface Sci.* **2006**, *301*, 703.
(11) Champion, J. A.; Katare, Y. K.; Mitragotri, S. *Proc. Natl. Acad. Sci. U. S. A.* **2007**, *104*, 11901.
(12) Bradley, L. C.; Stebe, K. J.; Lee, D. *J. Am. Chem. Soc.* **2016**, *138*, 11437.
(13) Seidel, S.; Riche, C.; Gupta, M. *Chemical Vapor Deposition of Polymer Films*. In *Encyclopedia of Polymer Science and Technology*, **2011**; doi: 10.1002/0471440264.pst467.
(14) Cheng, B. K.; Naccarato, B.; Kim, K. J.; Kumar, A. *Int. J. Heat Mass Transfer* **2016**, *102*, 154.
(15) Baghban, A.; Bahadori, M.; Rozyn, J.; Lee, M.; Abbas, A.; Bahadori, A.; Rahimali, A. *Appl. Therm. Eng.* **2016**, *93*, 1043.
(16) Leach, R. N.; Stevens, F.; Langford, S. C.; Dickinson, J. T. *Langmuir* **2006**, *22*, 8864.

(17) Enright, R.; Miljkovic, N.; Alvarado, J. L.; Kim, K.; Rose, J. W. *Nanoscale Microscale Thermophys. Eng.* **2014**, *18*, 223.
(18) Rose, J. W. *Int. J. Heat Mass Transfer* **1967**, *10*, 755.
(19) Ulrich, S.; Stoll, S.; Pefferkorn, E. *Langmuir* **2004**, *20*, 1763.
(20) Castillo, J. E.; Weibel, J. A.; Garimella, S. V. *Int. J. Heat Mass Transfer* **2015**, *80*, 759.
(21) Meakin, P. *Phys. Scr.* **1992**, *1992*, 31.
(22) Betz, A. R. *The Role of Droplet Dynamics in Condensation Frosting*. In *Ice Adhesion: Mechanism, Measurement and Mitigation*, Mittal, K. L.; Choi, C.-H., Scrivener Publishing LLC: Beverly, MA, **2020**, 135.
(23) Whitesides, G. M. Angew. Chem. Int. Ed. **2018**, *57*, 4258.
(24) Li, W.; Liu, Y.; Wu, M.; Feng, X.; Redfern, S. A. T.; Shang, Y.; Yong, X.; Feng, T.; Wu, K.; Liu, Z.; Li, B.; Chen, Z.; Tse, J. S.; Lu, S.; Yang, B. *Adv. Mater.* **2018**, *30*, 1800676.
(25) do E. S. Pereira, A.; Oliveira, H. C.; Fraceto, L. F. *Sci. Rep.* **2019**, *9*, 7135.
(26) Xu, W.; Lan, Z.; Liu, Q.; Du, B.; Ma, X. *Int. J. Heat Mass Transfer* **2018**, *127*, 44.
(27) Kim, S. H.; Noh, J.; Jeon, M. K.; Kim, K. W.; Lee, L. P.; Woo, S. I. *J. Micromech. Microeng.* **2006**, *16*, 526.
(28) Sun, Q. *Vib. Spectrosc.* **2009**, *51*, 213.
(29) Hosseinioun, A.; Nürnberg, P.; Schönhoff, M.; Diddens, D.; Paillard, E. *RSC Adv.* **2019**, *9*, 27574.
(30) Howell, N. K.; Arteaga, G.; Nakai, S.; Li-Chan, E. C. Y. *J. Agric. Food Chem.* **1999**, *47*, 924.
(31) Warwick, T., *Simultaneous IR and Raman Microscopy*, **2019**. https://blue-scientific.com/simultaneous-ir-raman/ (accessed June 06, 2023).
(32) Marshall, C. P.; Olcott Marshall, A. *Phil. Trans. R. Soc. A* **2010**, *368*, 3137.
(33) Karthik, G.; Premkumar, K.; Senthil Murugan, V. *J. Emerg. Technol. Innov. Res.* **2018**, *5*, 338.
(34) Hatcher, J. B.; Yost, D. M. *J. Chem. Phys.* **1937**, *5*, 992.
(35) Perrotta, A.; Christian, P.; Jones, A. O. F.; Muralter, F.; Coclite, A. M. *Macromolecules* **2018**, *51*, 5694.
(36) Rose, J. W. *Int. J. Heat Mass Transfer* **1976**, *19*, 1363.
(37) Mu, C.; Pang, J.; Lu, Q.; Liu, T. *Chem. Eng. Sci.* **2008**, *63*, 874.
(38) Ulrich, S.; Stoll, S.; Pefferkorn, E. *Langmuir* **2004**, *20*, 1763.
(39) Song, T.; Lan, Z.; Ma, X.; Bai, T. *Int. J. Therm. Sci.* **2009**, *48*, 2228.
(40) Kobayashi, Y.; Kuninaka, H. *J. Phys. Soc. Jpn.* **2022**, *91*, 084001.
(41) Zhao, H.; Beysens, D. *Langmuir* **1995**, *11*, 627.
(42) Harges, E.; Cremaschi, L.; Adanur, B. *Appl. Therm. Eng.* **2021**, *182*, 116052.
(43) Rose, J. W.; Glicksman, L. R. *Int. J. Heat Mass Transfer* **1973**, *16*, 411.
(44) Boroomandi Barati, S.; Pionnier, N.; Pinoli, J.-C.; Valette, S.; Gavet, Y. *Int. J. Therm. Sci.* **2018**, *124*, 356.
(45) McCormick, J. L.; Westwater, J. W. *Chem. Eng. Sci.* **1965**, *20*, 1021.
(46) Rose, J. W. *J. Enhanc. Heat Transf.* **2015**, *22*, 89.
(47) Xie, J.; Xu, J.; He, X.; Liu, Q. *Sci. Rep.* **2017**, *7*, 39932.
(48) Brain, P.; Butler, D. R. *Plant Cell Environ.* **1985**, *8*, 247.
(49) Xie, C.; Liu, G.; Wang, M. *Langmuir* **2016**, *32*, 8255.
(50) Unger, K.; Resel, R.; Coclite, A. M. *Macromol. Chem. Phys.* **2016**, *217*, 2372.
(51) Buback, M.; Kurz, C. H. *Macromol. Chem. Phys.* **1998**, *199*, 2301.
(52) Mei, M.; Yu, B.; Zou, M.; Luo, L. *Int. J. Heat Mass. Transfer* **2011**, *54*, 2004.
(53) Coclite, A. M.; Shi, Y.; Gleason, K. K. *Adv. Funct. Mater.* **2012**, *22*, 2167.